ADVANCED FUNCTIONAL MATERIALS
www.afm-journal.de

Overcoming the Challenges of Freestanding Tin Oxide-Based Composite Anodes to Achieve High Capacity and Increased Cycling Stability

*Florian Zoller, Sebastian Häringer, Daniel Böhm, Hannah Illner, Markus Döblinger, Zdeněk Sofer, Martin Finsterbusch, Thomas Bein, and Dina Fattakhova-Rohlfing**

Freestanding electrodes are a promising way to increase the energy density of the batteries by decreasing the overall amount of electrochemically inactive materials. Freestanding antimony doped tin oxide (ATO)-based hybrid materials have not been reported so far, although this material has demonstrated excellent performance in conventionally designed electrodes. Two different strategies, namely electrospinning and freeze-casting, are explored for the fabrication of ATO-based hybrid materials. It is shown that the electrospinning of ATO/carbon based electrodes from polyvinyl pyrrolidone polymer (PVP) solutions was not successful, as the resulting electrode material suffers from rapid degradation. However, freestanding reduced graphene oxide (rGO) containing ATO/C/rGO nanocomposites prepared via a freeze-casting route demonstrates an impressive rate and cycling performance reaching 697 mAh g^{-1} at a high current density of 4 A g^{-1}, which is 40 times higher as compared to SnO_2/rGO and also exceeds the freestanding SnO_2-based composites reported so far. Antimony doping of the nanosized tin oxide phase and carbon coating are thereby shown to be essential factors for appealing electrochemical performance. Finally, the freestanding ATO/C/rGO anodes are combined with freestanding $LiFe_{0.2}Mn_{0.8}PO_4$/rGO cathodes to obtain a full freestanding cell operating without metal current collector foils showing nonetheless an excellent cycling stability.

1. Introduction

Batteries and in particular lithium-ion batteries (LIBs) became an indispensable part of daily life. The fast-paced development of new portable electronic devices, electromobility, and large-scale energy storage demands LIBs with maximized capacities, advanced rate capability, and a persistent cycling performance. In order to address those issues new electrode materials are explored, implying in case of the anode that the currently used graphite with its rather low theoretical capacity of 372 mAh g^{-1} has to be replaced.[1–4]

SnO_2 attracted lots of attention as a promising alternative featuring a high theoretical capacity of 1494 mAh g^{-1} and a low working potential.[1–3,5] Lithiation and delithiation of SnO_2 can be subdivided into two main steps. In a first step, SnO_2 undergoes a conversion reaction resulting in the formation of metallic Sn embedded into a Li_2O matrix followed by alloying reactions between lithium and the previously formed Sn phase yielding Li_xSn ($0 \le x \le 4.4$).[2,3,5,6] However, the conversion reaction of macroscopic SnO_2 is irreversible, thus limiting the theoretical capacity to 782 mAh g^{-1} representing the capacity of the alloying step only.[6] Moreover, the conversion reaction, as well as the subsequent alloying reactions are accompanied by huge volume variations of up to 358% causing internal stress and a potential pulverization of the electrode. Nanosizing of SnO_2 is a well-known strategy to achieve reversibility of both conversion and alloying reactions and to accommodate the strong volume

F. Zoller, D. Böhm, M. Finsterbusch, D. Fattakhova-Rohlfing
Forschungszentrum Jülich GmbH
Institute of Energy and Climate Research (IEK-1): Materials Synthesis and Processing
Wilhelm-Johnen-Straße, 52425 Jülich, Germany
E-mail: d.fattakhova-rohlfing@fz-juelich.de

The ORCID identification number(s) for the author(s) of this article can be found under https://doi.org/10.1002/adfm.202106373.

DOI: 10.1002/adfm.202106373

F. Zoller, D. Fattakhova-Rohlfing
Faculty of Engineering and Center for Nanointegration Duisburg-Essen (CENIDE)
Universität Duisburg-Essen
Lotharstraße 1, 47057 Duisburg, Germany

S. Häringer, H. Illner, M. Döblinger, T. Bein
Department of Chemistry and Center for NanoScience (CeNS)
Ludwig-Maximilians-Universität München (LMU Munich)
Butenandtstrasse 5–13 (E), 81377 Munich, Germany

Z. Sofer
Department of Inorganic Chemistry
University of Chemistry and Technology Prague
Technická 5, 166 28 Prague 6, Czech Republic

changes.[6,7] The performance of SnO_2 based materials can be additionally enhanced by element doping, which increases the electrical conductivity up to several orders of magnitude.[3,8] A further increase of the overall electrical conductivity of the electrode can be achieved by embedding the (doped) SnO_2 nanoparticles into a carbonaceous support matrix that can be based on reduced graphene oxide (rGO), carbon nanotubes (CNTs), or carbon nanofibers (CNFs). Another positive effect of the carbonaceous matrix is its ability to alleviate the volume changes of SnO_2 during lithiation and delithiation enhancing consequently the overall electrochemical performance.[1,9–11] These effects can be further improved by introducing a carbon coating layer.[12–16] Such a carbon coating layer additionally prevents the SnO_2 particles from a direct contact with the electrolyte, which leads to decreased number of side reactions, thus improving the cycling stability.[15] Moreover, carbon coating is also reported to separate individual SnO_2/graphene sheets which can result in a higher accessibility of the active material reaching higher capacities.[12] Consequently, synergistic effects between nanosized doped SnO_2 particles, carbonaceous support materials, and the carbon coating layer can be expected resulting in an improved overall electrochemical performance.

Besides improving the storage capacity of individual electrode materials, the optimization of the battery design and the minimization of the fraction of electrochemically inactive components is another means to increase the total energy density of the battery. Electrodes for LIBs are generally prepared in slurry casting approaches, in which a suspension containing the active material or its respective composite, a polymeric binder, and conductive additives is coated onto a copper (anode) or aluminum (cathode) foil employed as current collector. Consequently, the electrodes consist of up to 50 wt% of electrochemically inactive materials, which decreases the overall energy density of the negative and positive electrode dramatically.[1] An attractive concept to reduce the amount of electrochemically inactive materials is the fabrication of so-called freestanding electrodes. Freestanding electrodes are based on conducting (mainly carbonaceous) materials that act simultaneously as current collector as well as conducting matrix incorporating and stabilizing the active material. Thus, freestanding electrodes have to face several challenges including a good electrical conductivity and sufficient mechanical stability to withstand the stress during the cell assembly and operation. Numerous SnO_2-carbon hybrid materials have been reported, which are partially applicable as freestanding electrodes. The reported examples of freestanding electrodes include SnO_2 embedded into rGO,[1,10,11,17–22] CNTs,[9,23,24] CNFs,[25–28] carbon cloth,[5,29–31] carbon paper,[32] or carbon monoliths,[33] which have been prepared via electrospinning,[25] vacuum filtration,[1,11,19,22,23] a combination of in-situ hydrothermal synthesis and freeze-drying,[10,18] hydrothermal synthesis of SnO_2 on a preformed array,[5,29,30] or electrodeposition[32]. In contrast to the pure SnO_2-based freestanding electrodes, their doped analogues are much less investigated, although published examples demonstrate the clear benefits of this approach for the electrode performance. Thus, Zhang et al. reported a Co doped SnO_2/rGO/carbonized cotton composite that demonstrated a better conductivity and a superior electrochemical performance as compared to the undoped equivalent.[31] In another publication, Zhang et al. described a Fe doped SnO_2/rGO/carbonized cotton composite. The performance of this material was also superior to that of an undoped equivalent, but slightly inferior compared to the freestanding Co doped SnO_2 composite.[34] The Zn doped SnO_2/rGO composite reported by Dou et al. is another example for combining doped SnO_2 and a current collector-free electrode architecture with a beneficial effect on the electrochemical performance.[35]

Sb doped SnO_2 (ATO) freestanding composites have not been reported so far, despite the fact that conventional Sb:SnO_2 composite coated onto Cu foil electrodes have demonstrated excellent rate and cycling stability superior to that of other SnO_2-based materials.[2,36,37]

In this paper we have investigated different ways to prepare freestanding binder-free ATO/rGO electrodes. Two approaches were tested that are industrially applicable due to their scalability and are commonly used for freestanding electrode fabrication, namely freeze-casting and electrospinning. However, in our case the fabrication of ATO/carbon electrodes by electrospinning with polyvinyl pyrrolidone polymer (PVP) was not possible, as the pyrolysis step required to carbonize the fiber forming PVP employed in the spinning solution results in a reduction of ATO with a formation of poorly performing SbSn-alloy/carbon nanofiber (SbSn/CNF) composites. In contrast, freeze-casting enables the fabrication of freestanding ATO/C/rGO electrodes with a good rate performance and cycling stability due to a multi-step synthesis procedure compatible with the employed precursor solution resulting in a carbon coated rGO composite with a homogenously dispersed nanosized ATO phase.

Finally, a freestanding full cell was produced, consisting of the freestanding ATO/C/rGO nanocomposite as an anode and a high voltage freestanding $LiFe_{0.2}Mn_{0.8}PO_4$/C/rGO (LFMP/C/rGO) electrode as a cathode. The ATO/C/rGO–LFMP/C/rGO LIB cell reveals an excellent cycling stability at 1C reaching 116 mAh g^{-1}_{LFMP} (based on the weight of LFMP) in the 175th cycle showing practically no capacity fading.

2. Results and Discussion

Two different strategies were evaluated for the preparation of freestanding Sb doped SnO_2/carbonaceous hybrid materials.

In the first approach, Sb doped SnO_2/graphene oxide (ATO/GO) nanocomposites (Figure S1, Supporting Information, left) were prepared in a freeze-casting approach. In the first step, a basic (pH = 9) suspension containing tin (IV) chloride, antimony (III) chloride, and GO was prepared. As follows from the previous reports, tin and antimony precursors hydrolyze with the formation of different tin hydroxides including for example $[Sn(H_2O)_{6-x}(OH)_x]^{(4-x)+}$ species. The charged hydrolyzed species can interact with the hydroxyl, carboxyl, and epoxy functional surface groups of GO which are detectable by FT-IR (Figure S2, Supporting Information), resulting in a homogenous deposition of the amorphous ATO precursor on the surface of GO, which transforms to the crystalline ATO.[38,39] After repeated extensive washing and centrifugation, the ATO/GO composite was treated by ultrasonication forming a homogenous suspension. The suspension was subsequently freeze-cast and freeze-dried, resulting in dark yellowish/brownish ATO/GO monoliths (Figure S1, Supporting Information, left) with a diameter

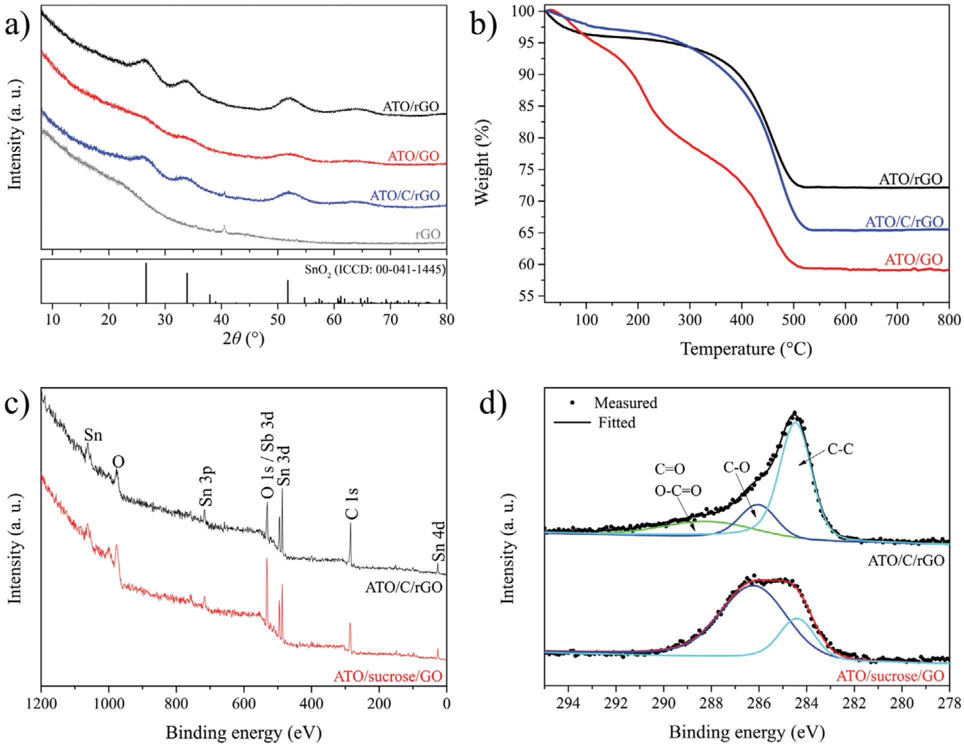

Figure 1. a) XRD patterns of ATO/rGO, ATO/GO, ATO/C/rGO, and rGO. Bars in the box at the bottom mark the tetragonal SnO_2 (cassiterite) positions (ICDD card No. 00-41-1445). b) TGA of ATO/GO, ATO/rGO, and ATO/C/rGO. c) XPS survey spectra and d) C1s region of ATO/C/rGO and ATO/sucrose/GO.

of ≈3.5 cm. After pyrolysis at 400 °C in nitrogen, black ATO/rGO nanocomposite monoliths (Figures S1, middle, and S3, Supporting Information) are obtained. Further freestanding composite electrodes were prepared via a slightly modified route including the addition of different amounts of sucrose during the ultrasonication step to yield carbon coated ATO/rGO nanocomposites (labeled as ATO/C/rGO and ATO/C-2/rGO, with C-2 indicating the double amount of sucrose added in comparison to ATO/C/rGO). The additional carbon coating is thereby expected to improve the cycling stability and rate performance of SnO_2-based composite materials.[9,14,15]

The successful formation of phase-pure crystalline ATO nanoparticles inside the hybrid composites is confirmed by XRD (**Figure 1**a). The three diffraction peaks at 26.6, 33.9, and 51.8° 2θ can be assigned to the (110), (101), and (211) reflections of tetragonal SnO_2 (ICDD card No. 00-41-1445). The average crystalline domain size of the ATO nanoparticles of the ATO/GO composite is estimated to be ≈1.0 nm, based on the broadening of the (211) peak evaluated by using Scherrer's equation.[24] Even after pyrolysis, only a minor domain growth with an estimated average diameter of 2.0 nm is observed. Interestingly, the addition of sucrose during ultrasonication impedes the ATO particle growth upon subsequent pyrolysis resulting in average domain sizes of only 1.7 and 1.4 nm for the ATO/C/rGO and ATO/C-2/rGO composites (Figure 1a and Figure S4a, Supporting Information) according to the XRD peak broadening. In case of the undoped SnO_2/rGO nanocomposites, an average particle size of 2.1 nm was observed. Thermogravimetric analysis (TGA) of the hybrid materials reveals that ATO nanoparticles have a share of ≈75 wt% in the freestanding ATO/rGO composite (Figure 1b). Moreover, TGA identifies that GO has been successfully reduced to rGO during the pyrolysis step at the applied temperature of 400 °C, as only one major weight loss step between 400 and 500 °C was observed in the TGA, which is attributed to the combustion of rGO under air atmosphere.[39] In comparison, ATO/GO features additional weight loss steps at 220 °C related to the loss of oxygen containing groups on the surface of GO.[40] The weight fraction of the ATO phase in the ATO/C/rGO and ATO/C-2/rGO composites is much lower, equaling 65 and 54 wt%, respectively, due to the additional carbon coating (Figure 1b and Figure S4b, Supporting Information).

The successful reduction of GO is also confirmed by the results obtained from FT-IR analysis (Figure S2, Supporting Information). In the case of GO and the respective ATO and SnO_2 containing composites, a large broad peak at ≈3300 cm^{-1} is visible which can be assigned to O—H stretching vibrations of adsorbed water molecules and structural —OH groups.[41] Moreover, the peaks at 1636, 1420, 1060, and 968 cm^{-1} are attributed to bending vibration of —OH groups, and to the vibrations of carboxyl and epoxy functional groups, respectively.[42,43] ATO/sucrose/GO composites display additional peaks between 1200 and 860 cm^{-1} related to sucrose. These peaks vanish or at least drastically decrease in intensity after the pyrolysis step. Additionally, two new peaks are clearly visible at 1560 and 1220 cm^{-1}. The former indicates a C=C stretching and skeletal vibration of the rebuilt graphene structure.[39,41,44] The latter is assigned to residual epoxy groups on the surface of rGO and can be commonly found for rGO and rGO containing composite materials as reported in literature.[10,39,43,44]

ATO/sucrose/GO and ATO/C/rGO nanocomposite were also studied by X-ray photoelectron spectroscopy (XPS). The survey XPS spectra depicted in Figure 1c confirms the presence of C, O, Sn, and Sb. Evaluation of the C 1s peak (Figure 1d) before (ATO/sucrose/GO) and after pyrolysis (ATO/C/rGO) reveals a severe decrease of the peak related to C—O containing groups which is a clear indication for the successful reduction of GO to rGO and the carbonization of sucrose, hence supporting the results of TGA and FT-IR analysis. The Sn 3d peak (Figure S5a, Supporting Information) is composed of two peaks at 495.2 and 486.8 eV which can be assigned to Sn $3d_{3/2}$ and Sn $3d_{5/2}$, respectively. Those binding energies are in the range typically associated with Sn^{4+}, which additionally supports the presence of a SnO_2 phase.[13] Doping of tin oxide with antimony can be confirmed by XPS, as well. Antimony is mostly in the valence state Sb^{5+} (Figure S5b, Supporting Information) which indicates an enhanced electrical conductivity as Sb^{5+} ions act as donor species; in contrast Sb^{3+} ions are known as electron traps.[2,8]

Nitrogen sorption measurements were conducted to analyze the porosity of the freestanding hybrid materials. As depicted in Figure S6, Supporting Information, the composites display type IV isotherms with H2-type hysteresis loops, which is typically ascribed to mesoporous materials. Analysis of the pore size distribution based on density functional theory (DFT) methods and a slit/cylindrical pore model (SnO_2/rGO and ATO/rGO) or a slit pore model (ATO/C/rGO and ATO/C-2/rGO) reveals a maximum ranging between 20–50 nm, as shown in the insets of Figure S6, Supporting Information, which further indicates a mesoporous structure of the hybrid materials. The total pore volume of the nanocomposites is dependent on the amount of the additionally added sucrose. The ATO/rGO showed a total pore volume of 0.156 $cm^3\ g^{-1}$, which decreased to 0.135 and 0.052 $cm^3\ g^{-1}$ for ATO/C/rGO and ATO/C-2/rGO, respectively. A similar correlation is also obtained for the Brunauer–Emmett–Teller (BET) specific surface area. The nanocomposites without an additional carbon coating showed BET surface areas in the same range equaling to 179 and 163 $m^2\ g^{-1}$ for SnO_2/rGO and ATO/rGO, respectively. In case of the carbon-coated hybrid materials the BET surface area is significantly decreased to 60 $m^2\ g^{-1}$ for ATO/C/rGO and to 21 $m^2\ g^{-1}$ in case of ATO/C-2/rGO. Porosity and a large specific surface area are beneficial with regard to a high contact area between the active material and the electrolyte, enabling rapid charge transfer and hence an improved electrochemical performance.[30,39] However, large surface areas can be also disadvantageous, possibly leading to a large number of unwanted side reactions.[45] Therefore, we assume a medium surface area as exhibited by the ATO/C/rGO composite with moderate sucrose content to represent a suitable tradeoff.

The morphology of the freestanding nanocomposites was analyzed by scanning electron microcopy (SEM). The cross-sectional images of the three ATO/rGO based nanocomposites (**Figure 2**) reveal that the rGO sheets form an interconnected 3D network homogenously coated by the inorganic ATO phase. Such a spongy structure with its open channels can be very beneficial for infiltration with electrolyte throughout the composite electrode ensuring a maximized wetting and electrode electrolyte interface area shortening the Li^+ diffusion pathways. Moreover, the fluffy structure can also be advantageous for alleviating the volume changes of the ATO phase upon de/-lithiation.[39]

Interestingly, the addition of sucrose affects the overall morphology of the hybrid material. With increasing sucrose amount, the composite consists of more wrinkled and contracted ATO-coated rGO sheets in comparison to the rather flat rGO sheets in case of the ATO/rGO composite (Figure 2b,d,f). These observations also correlate with the decreasing BET surface area upon the sucrose addition. Moreover, the morphology of the ATO/rGO composites (with and without carbon coating) differs also from that of pure rGO obtained by the same freeze-casting procedure. Pure rGO monoliths feature a more crumpled-paper like structure (Figure S7e,f, Supporting Information).

The homogenous distribution of ATO particles onto rGO sheets is visible in the SEM/EDX elemental maps (Figure S8, Supporting Information), where Sn and Sb signals are co-localized with the C signals originating from rGO. Further evidence of a homogenous coverage of the rGO sheets by inorganic phase nanoparticles is given by a comparison of identical location SEM images acquired with a morphology contrast (secondary electron)-based versus an increased material contrast (back-scattered electrons)-based detector (Figure S9, Supporting Information). Inorganic ATO nanoparticles thereby exhibit an increased intensity (in Figure S9b, Supporting Information) compared to the underlying carbonaceous matrix due to an increased Z-contrast in the imaging mode. The Sb doping ratio inside the SnO_2 particles is ≈8 to 10 at% according to EDX data (Figure S8e, Supporting Information).

Transmission electron microcopy (TEM) and high-resolution transmission electron microcopy (HRTEM) of the ATO/rGO, ATO/C/rGO, and ATO/C-2/rGO nanocomposites (**Figure 3**a,b,d,e and Figures S10 and S11, Supporting Information) furthermore shows a homogenous distribution of the ATO nanoparticles on the rGO sheets. Sheets aligned perpendicular to the TEM grid are indicated by red arrows in Figure 3b. HRTEM of the nanoparticles in the ATO/rGO and ATO/C/rGO hybrid materials reveal their crystallinity (Figure S10, Supporting Information), with lattice spacing of ≈0.34 nm corresponding to the (110) lattice plane of ATO. These results agree with the values obtained from the selected area electron diffraction (SAED) pattern. The patterns of all three composites show diffraction rings (Figure 3c,f and Figure S11c, Supporting Information), which can be assigned to the cassiterite structure of ATO (*d*-values: 3.4 (110), 2.7 (101), and 1.8 Å (211)) indicating the formation and random orientation of nanocrystalline ATO particles on the surface of rGO.[2,39,46] The additional ring at ≈2.1 Å, which is detectable in all ATO/rGO based composites, can be attributed to rGO.[2,17,47] In case of the carbon coated ATO/rGO composites (ATO/C/rGO and ATO/C-2/rGO), the rings attributed to ATO are broader and less pronounced. The former is related to a smaller crystallite size with increasing carbon content, in agreement with the results obtained by XRD. The latter is related to an increasing background with increasing carbon content. Additionally, the size of ATO particles was evaluated from the TEM images depicted in Figure 3 and Figures S10 and S11, Supporting Information. The resulting particle size distributions (Figure S12, Supporting Information) show a similar trend in comparison to the average domain sizes calculated from XRD; the ATO particles decrease in size with increasing carbon content. The larger discrepancies between particle size (TEM) and average domain size (XRD) are observed for the

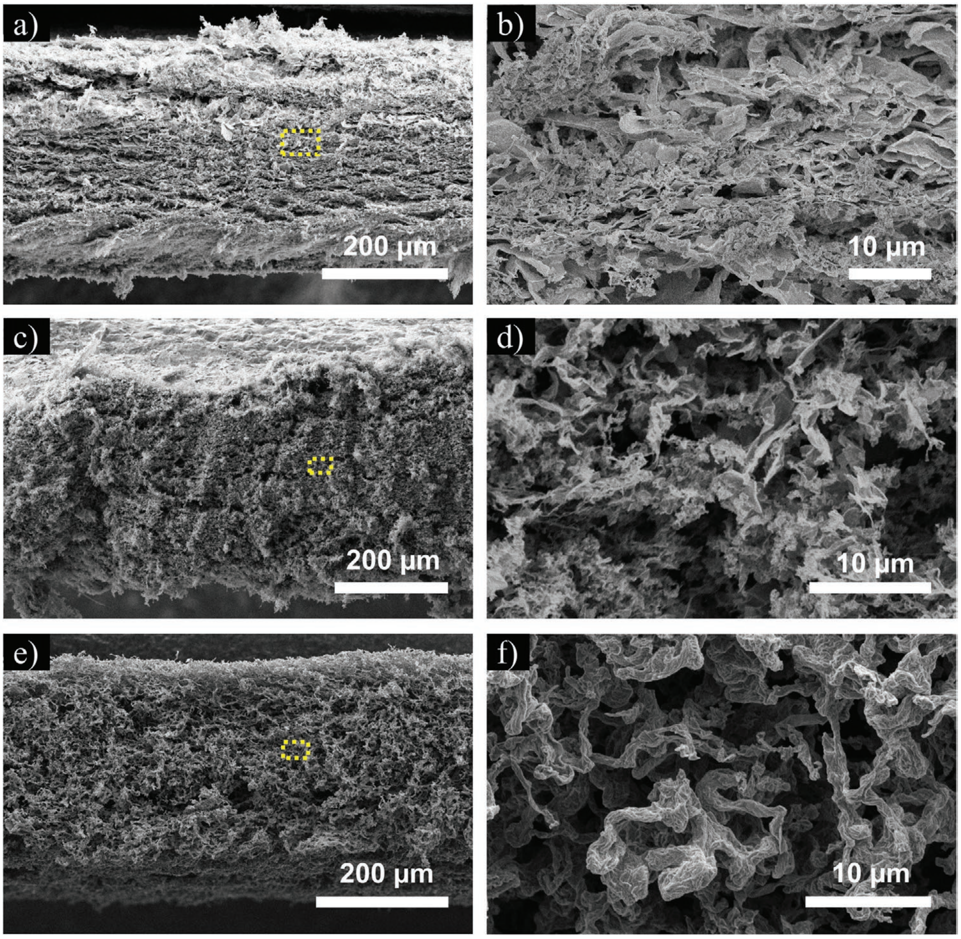

Figure 2. SEM images of cross sections (a,c,e) and magnification of the corresponding marked areas (b,d,f) of freestanding ATO/rGO (a,b), ATO/C/rGO (c,d), and ATO/C-2/rGO nanocomposites (e,f).

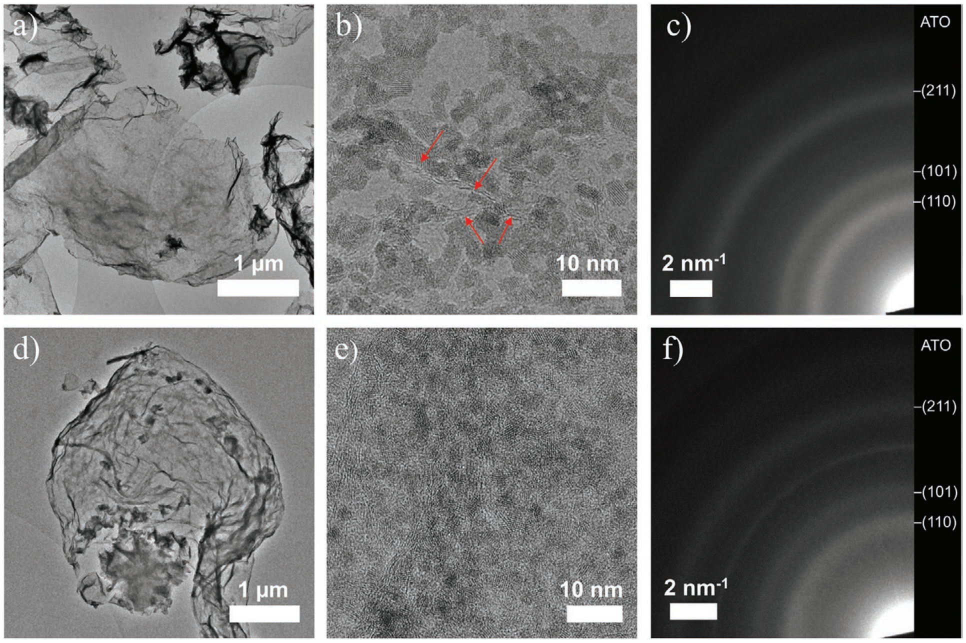

Figure 3. TEM images (a,b,d,e) and SAED patterns (c,f) of ATO/rGO (a–c) and ATO/C/rGO (d–f) nanocomposites. The red arrows in b) mark rGO sheets aligned perpendicularly to the TEM grid. The rings in the SAED patterns (c,f) are assigned to the tetragonal structure of the ATO nanoparticles.

carbon-coated materials probably due to the presence of carbon, which makes the determination of particle size in TEM less straightforward. In general, XRD analysis by using the Scherrer equation provides the average size of crystalline domain while TEM enables to determine the size of individual nanoparticles, but the information is less statistically representative. Particle and domain size analysis must not result in the same values. However, in total the particle sizes obtained by both methods are in a rather good agreement.

Different freestanding composites demonstrate similar electrical conductivity in the range from 2.3 to 5.2 × 10^1 S cm^{-1} indicating a minor influence of the carbon coating on the overall conductivity. However, it cannot be excluded that the carbon coating increases the electrical conductivity locally around the ATO particles, thus improving the electrochemical performance.

In a second synthesis approach presented in this work, we have attempted to prepare ATO/carbon nanofiber (ATO/CNF) freestanding composite electrodes by the electrospinning of an ethanolic spinning solution containing tin acetate, antimony acetate, and polyvinyl pyrrolidone (PVP). The resulting flexible and mechanically stable mat has a size of ≈10 × 25 cm (Figure S13a, Supporting Information) and consists of homogenous nanofibers with diameters of ≈250 nm (Figure S13b, Supporting Information) and a length of hundreds of micrometers and more. EDX analysis reveals a uniform distribution of Sn and Sb along the PVP nanofibers and an intended Sb amount of 10 at% in context to Sb:SnO_2 (Figure S14, Supporting Information). After stabilizing the composite mat in air, three very small broad bumps are observed at ≈26.6°, 33.9°, and 51.8° 2θ in the corresponding XRD pattern, which can be assigned to the (110), (101), and (211) reflections of SnO_2 (ICCD card No. 00-041-1445), respectively, showing the formation of ATO.[2] In order to obtain a conductive framework, the composite has to be pyrolyzed to carbonize the PVP fibers. Different pyrolysis temperatures were tested ranging from 400 to 700 °C. Besides the diffraction peaks assigned to SnO_2, additional reflections arise at a pyrolysis temperature of 400 °C that can be assigned to a SnSb-alloy (ICCD card No. 00-033-0118) and Sn (ICCD card No. 00-004-0673). With increasing temperature, the diffraction peaks of SnO_2, SnSb, and Sn get sharper and gain in intensity, indicating an increase in crystallinity and growth of crystalline domain sizes. At a pyrolysis temperature of 700 °C, no diffraction peaks of the cassiterite phase (ATO) were detected, indicating a complete reduction to metallic Sn and SnSb (**Figure 4**a), most probably due to a reducing environment generated by the carbonization of PVP.[48] Chen et al. observed a similar effect with a reported reduction of a Mo:SnO_2/polyacrylonitrile (PAN) composite to a Mo:Sn/CNF hybrid upon pyrolysis at 700 °C.[7]

Moreover, pyrolysis of the Sb:SnO_2/PVP composites at different temperatures also resulted in different morphologies. After pyrolysis at 400 °C, the surface of the nanofibers appears to be rougher (Figure 4b) as compared to the non-pyrolyzed raw material (Figure S13b, Supporting Information). At 500 °C additional small particles are visible at the surface of the nanofibers that increase drastically in size with increasing pyrolysis temperature (Figure 4b–e), which is furthermore in good agreement with increasingly sharp peaks visible in corresponding XRD patterns.

The SbSn/CNF composites pyrolyzed at 400–700 °C were analyzed by cyclic voltammetry (Figures S15 and S16a, Supporting Information) and galvanostatic charge/discharge measurements (Figure S16b, Supporting Information). As the composites were still maintained as paper-like mats after pyrolysis, they were used directly as freestanding electrode materials.

The results of electrochemical characterization of the SbSn/CNF composites, as discussed in the supporting information,

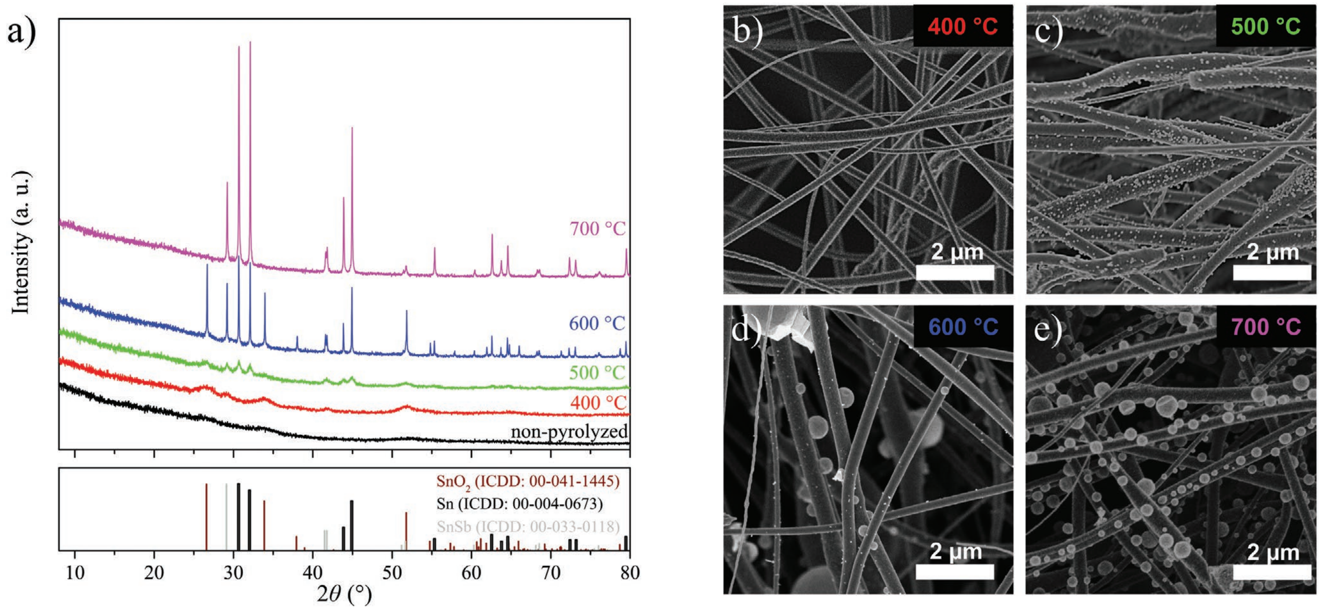

Figure 4. a) XRD patterns of electrospun non-pyrolyzed ATO/PVP and of the corresponding composites obtained after pyrolysis at 400, 500, 600, and 700 °C and b–e) the respective SEM images.

suggest that they are not well suited for the application in LIBs. We assume that the poor performance of the composites pyrolyzed at 400 and 500 °C is due to the incomplete carbonization of PVP. The higher temperatures not only lead to a targeted carbonization of PVP but also to a non-desired reduction of ATO to Sn/Sb particles of up to several hundred nanometers in size as indicated in Figure 4. The particles are not embedded in the CNF fibers probably leading to an irreversible agglomeration and loss of active material upon cycling.

In contrast to the freestanding electrospun electrodes that feature low capacities and fast capacity fading, the ATO/rGO nanocomposites prepared by freeze-casting reveal a greatly improved and stable electrochemical behavior as shown in the following section. The nanocomposites were directly used as freestanding electrodes without the help of a copper foil current collector, polymeric binder, or supplementary conductive additives.

In order to study the different reactions taking place during lithiation and de-lithiation, the freestanding ATO/rGO, ATO/C/rGO, ATO/C-2/rGO, SnO_2/rGO, SnO_2/C/rGO, and rGO materials were analyzed using cyclic voltammetry in a potential range of 0.01 to 3.0 V versus Li/Li^+ at a scan rate of 0.2 mV s^{-1} (**Figure 5**a and Figure S17, Supporting Information).

During the first cycle a distinct cathodic peak at ≈1.0 V versus Li/Li^+ is observed for the ATO/C/rGO composite electrode (Figure 5a), which is also detectable as a voltage plateau in the respective galvanostatic discharge curves (Figure 5b). This feature is typical for SnO_2-based compounds and corresponds to the conversion reaction of ATO nanoparticles to Sn and Sb as well as Li_2O. During the first scans this process is accompanied by an irreversible formation of a solid electrolyte interface (SEI) layer, which results in significant capacity losses during the first cycles.[2,49] Furthermore, a small shoulder at 0.5 V versus Li/Li^+ and an intense peak at 0.04 V versus Li/Li^+ can be observed during the first reduction scan, which correspond to the multistep alloying reactions between Sn/Sb and lithium ions with formation of $Li_{4.4}Sn$ and Li_3Sb alloys.[2,42,50] The peaks at 0.6 and 1.3 V versus Li/Li^+ observed during the reverse anodic scan correspond to the dealloying reaction and the conversion of Sn/Sb back to ATO.[42] Similar CV curves are also obtained for the SnO_2/rGO, SnO_2/C/rGO, ATO/rGO, and ATO/C-2/rGO hybrid materials (Figure S17a–d, Supporting Information).

Figures 5c and d display the change in capacity of the ATO/rGO, ATO/C/rGO, ATO/C-2/rGO, SnO_2/rGO, and SnO_2/C/rGO electrodes during multiple galvanostatic charge/discharge and at different rates, respectively. The charge and discharge capacities, as well as the discharging/charging current densities discussed in the following are based on the weight of the entire electrode, including the mass of ATO/SnO_2, rGO, and carbon coating.

The cycling measurements (Figure 5c) were conducted at a discharge and charge current of 1 A g^{-1}. In the first cycle, the freestanding ATO/rGO composite reaches discharge and charge capacities of 1260 and 659 mAh g^{-1}, respectively, corresponding to a Coulombic efficiency of 52%. The low initial Coulombic efficiency is assigned to the formation of a SEI layer as discussed above. In the subsequent cycles stable Coulombic efficiencies approaching 100% were obtained. The discharge

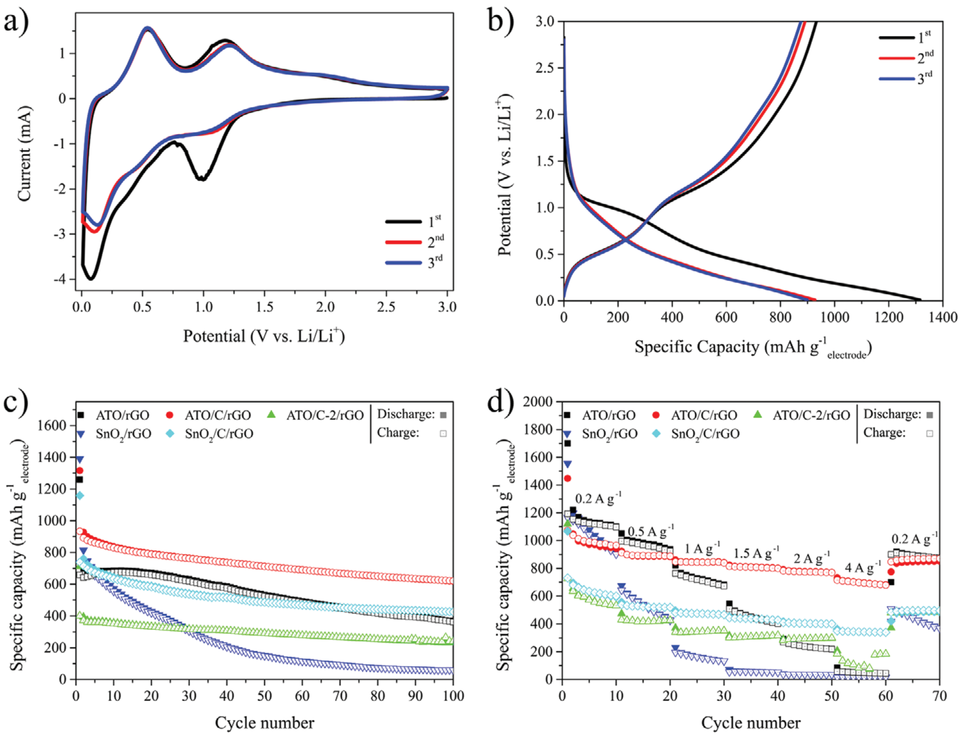

Figure 5. a) CV curves of freestanding ATO/C/rGO recorded in the potential range between 0.01 and 3.0 V versus Li/Li^+ at a scan rate of 0.2 mV s^{-1} and b) the corresponding charge/discharge curves at 1 A g^{-1}. c) Cycling stability at 1 A g^{-1} and d) rate performance at current densities ranging from 0.2 to 4 A g^{-1} of freestanding ATO/rGO, ATO/C/rGO, ATO/C-2/rGO, SnO_2/rGO, and SnO_2/C/rGO composites.

and charge capacity values however slightly decrease resulting in capacities of 365 and 362 mAh g^{-1} after 100 cycles, respectively. In case of the undoped SnO_2/rGO composite, capacity fading is even more pronounced. After 100 cycles a reversible capacity of only 60 mAh g^{-1} is retained demonstrating the benefits of antimony doping, which increases the reversibility of the conversion reaction and enhances the conductivity of SnO_2 particles.[2,3,37]

In case of the carbon-coated SnO_2/C/rGO composite, a clear enhancement of the cycling stability can be detected when compared to SnO_2/rGO. This is ascribed to the stabilization effect of the carbon coating layer. The advantage of using both carbon coating and antimony doping is demonstrated by the ATO/C/rGO composites. The ATO/C/rGO composites with a sucrose-derived carbon amount of 13 wt% demonstrated a drastically improved cycling stability as compared to the uncoated equivalent. In the first cycle, discharge and charge capacities of 1316 and 933 mAh g^{-1} are reached, respectively, corresponding to a Coulombic efficiency of 71%, which increases in the following cycles to almost 100%. After 100 cycles a reversible capacity of 620 mAh g^{-1} is retained, which is almost two times as high as in the case of conventional graphite anodes. The improved stability as compared to ATO/rGO can be explained by the newly introduced carbon coating layer which is known to enhance the contact between ATO nanoparticles and rGO sheets upon cycling, thus enabling fast electron transfer, increasing the overall conductivity, stabilizing the large volume changes of the ATO particles during cycling, and also preventing the Sn, Sb, and SnSb nanoparticles from aggregation.[11,14,15,50,51] Moreover, comparison of the carbon-coated ATO/C/rGO and SnO_2/C/rGO composites indicates that antimony doping can lead to higher reversible capacities which may be caused by a better conductivity inside the ATO nanoparticles and an improved reversibility of the electrochemical reactions.

ATO/C-2/rGO electrodes with an additionally increased amount of sucrose-derived carbon (28 wt%) show an even slightly better cycling stability, but significantly lower capacities as compared to the ATO/C/rGO electrodes. The charge capacities of ATO/C/rGO electrodes are 401, 360, and 242 mAh g^{-1} in the 1st, 5th, and 100th cycle, respectively. The lower capacity values of the ATO/C-2/rGO electrode are mainly attributed to the lower fraction of ATO in the electrode due to the increased amount of carbon. Moreover, the different morphologies of the ATO/rGO, ATO/C/rGO, and ATO/C-2/rGO composites (Figure 2) can also have an impact on their respective electrochemical behavior. The crumpled structure with its slightly agglomerated rGO sheets and the lower surface area of ATO/C-2/rGO may limit the accessibility of the ATO particles, which could thereby explain a decreased capacity as compared to the bare ATO/rGO as well as to the optimized carbon coated ATO/C/rGO nanocomposite.

The cycling stability of the most promising freestanding ATO/C/rGO electrodes was additionally evaluated at a higher current density of 2 A g^{-1}, with three preconditioning cycles at 0.2 A g^{-1} in advance (Figure S18, Supporting Information). The initial low current density cycles were conducted to assure the formation of a stable and homogenous SEI which can result in a favorable stable cycling behavior. After the preconditioning cycles, the composite reached reversible capacities of 750 mAh g^{-1}. After 1000 cycles at a high current density of 2 A g^{-1}, the freestanding ATO/C/rGO composite still maintained a reversible capacity of 423 mAh g^{-1} indicating a significant cycling stability even at high current densities.

The rate performance of the freestanding electrodes was evaluated at different charging and discharging current densities ranging between 0.2 and 4 A g^{-1} (Figure 5d). For low current densities, ATO/rGO and SnO_2/rGO demonstrate the highest specific capacities due to a larger fraction of active material as compared to the carbon coated ATO/C/rGO and ATO/C-2/rGO nanocomposites. With increasing current densities, however, the situation reverses, and the capacity of carbon-coated composites greatly outperforms that of the non-coated electrodes. The ATO/C/rGO composite reached 991, 892, 844, 808, 774, and 697 mAh g^{-1} (in the 5th cycle of each individual rate step) at 0.2, 0.5, 1, 1.5, 2, and 4 A g^{-1} respectively. When the current density was set back to 0.2 A g^{-1}, the freestanding ATO/C/rGO composite retained 870 mAh g^{-1}, corresponding to a capacity retention of 81% compared to the 1st cycle. The ATO/C-2/rGO demonstrated a similarly appealing rate performance, however accompanied by a distinctly lower specific capacity values as compared to ATO/C/rGO which matches with the findings obtained in the cycling stability measurements. These results demonstrate both the advantage of introducing Sb as dopant and using an appropriate carbon coating layer to achieve an excellent rate performance even at a high current density of 4 A g^{-1}.

Compared with other freestanding (doped) SnO_2 composites reported in the literature (see Table S2, Supporting Information), a superior rate performance of the freestanding ATO/C/rGO electrode prepared by freeze-casting presented in this work can be observed. Among them, the best performing freestanding SnO_2/graphene composite electrodes with SnO_2 particle sizes of 3–5 nm prepared by Gao et al. exhibited a reversible capacity of 1020 and 467 mAh g^{-1} at 0.2 and 4 A g^{-1}, respectively.[10] Our best performing freestanding ATO/C/rGO nanocomposite with smaller active size nanoparticles of ≈1.7 nm reached a similar specific capacity at the low current density and an almost 50% higher value at 4 A g^{-1}. We attribute the better performance of our freestanding ATO/C/rGO nanocomposite especially to the synergistic effects between Sb doping, ultrasmall particle sizes, and the utilization of a carbon coating layer.

Nyquist plots derived from electrochemical impedance spectroscopy (EIS) of SnO_2/rGO, ATO/rGO, and ATO/C-2/rGO electrodes (Figure S19, Supporting Information) show a semicircle in the high frequency region with a diameter corresponding to the charge transfer resistance at the electrode–electrolyte interphase. The slope in the lower frequency regime described by the Warburg impedance is thereby related to the Li^+ diffusion through the electrode material.[39,42] Upon doping the charge transfer resistance decreases significantly, which is attributed to the increased conductivity inside the ATO nanoparticles.[8] The charge transfer resistance (R_{CT}) of carbon coated and uncoated ATO/rGO composites is very similar; the smallest resistance was however observed for the ATO/C/rGO nanocomposite indicating the most favorable charge transfer kinetics. Additionally, lithium-ion diffusion coefficients (D_{Li+}) of the freestanding composites were calculated from EIS data using the following equations:[11,13,51]

$$Z' = R_S + R_{CT} + \sigma_W \omega^{-0,5} \tag{1}$$

$$D_{Li^+} = \frac{R^2 T^2}{2A^2 n^4 F^4 C^2 \sigma_W^2} \tag{2}$$

where Z' is related to the real part of the impedance, R_S is the electrolyte resistance, R_{CT} represents the charge transfer resistance, σ_W is the Warburg impedance coefficient, ω is the angular frequency, D_{Li+} is the lithium-ion diffusion coefficient, R is the gas constant (8.314 J mol^{-1} K^{-1}), T is the temperature (298 K), A is the surface area of the electrode (in this paper the geometrical surface area of 2.54 cm^2 was used for simplicity), n is the number of electrons participating per formula unit, F is the Faraday constant (96 485 C mol^{-1}), and C is the concentration of lithium ions in the electrode (1.15 м).

The Warburg impedance coefficient equals to the slope of the linear relationship between Z' and $\omega^{-0.5}$ in the low frequency region depicted in Figure S19b, Supporting Information. The resulting D_{Li+} values are summarized in Table S1, Supporting Information. It can be clearly seen that both doping and carbon coating are beneficial for obtaining high lithium-ion diffusion coefficients resulting in 3.35×10^{-10} cm^2 s^{-1} in case of the ATO/C/rGO. These results are also in good agreement with rate performance and cycling stability measurements.

In order to evaluate possible changes in morphology upon cycling, the Sb-doped freestanding composites ATO/rGO, ATO/C/rGO, and ATO/C-2/rGO were analyzed after 100 cycles at 1 A g^{-1} (Figure 5c) by XRD, SEM, and TEM measurements (**Figure 6**, Figures S20 and S21, Supporting Information). Prior to analysis the electrodes were washed with dimethyl carbonate to remove electrolyte residues. XRD analysis of the three composites reveals that the diffraction peaks associated with the SnO_2 rutile structure disappear after cycling. However, in case of ATO/rGO small peaks at 30.6° and 40.3° 2θ evolved which can be assigned to Sn (ICDD card No. 01-071-3772). Nevertheless, Sn and Sb are still present and highly distributed in all composites as proven by SEM/TEM-EDX measurements. Interestingly the morphology changed differently upon cycling for the coated and uncoated ATO based composites as evidenced by SEM analysis. In case of ATO/rGO larger agglomerates are visible on the surface of the rGO sheets, whereas for ATO/C/rGO a lot of small species can be detected and for ATO/C-2/rGO a more melt-like surface coverage (Figure 6 and Figure S20, Supporting Information) can be observed. Therefore, it can be speculated that, in addition to the increase in the local electronic conductivity, carbon coating confines the irreversible morphology changes accompanying the phase transformations in conversion/alloying-type electrodes, thus increasing the cycling stability of the ATO-based anodes.

Finally, the freestanding ATO/C/rGO composites were analyzed in a full cell configuration using a high-voltage freestanding $LiFe_{0.2}Mn_{0.8}PO_4$/C/rGO composite as a cathode (**Figure 7**). Synthesis, characterization, and half-cell performance of the freestanding LFMP/C/rGO nanocomposite can be found in our previous publication.[52] The rate performance and the cycling stability measurements of the full cells were conducted between 2.0 and 4.5 V versus Li/Li$^+$. The observed capacity values are based on the mass of cathodic LFMP.

The rate performance of the freestanding ATO/C/rGO–LFMP/C/rGO LIB cell was evaluated at different C-rates

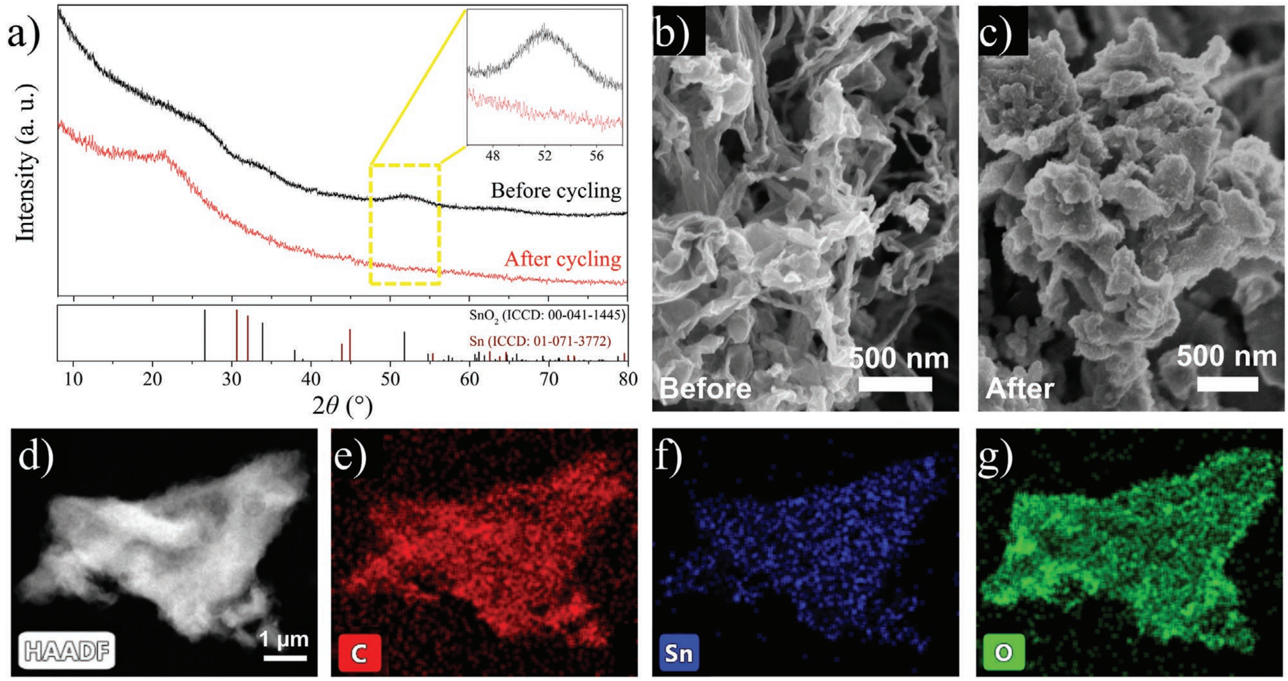

Figure 6. a) Ex situ analysis of ATO/C/rGO after 100 cycles at 1 A g^{-1} by XRD, c) SEM in comparison to uncycled ATO/C/rGO (XRD (a) and SEM (b)). d) STEM image of ATO/C/rGO after cycling in HAADF mode and e–g) the corresponding EDX mapping micrographs.

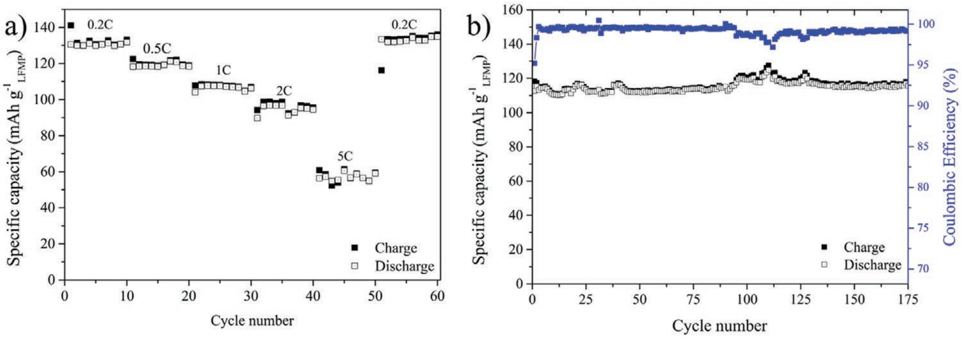

Figure 7. a) Rate performance, b) cycling stability (1C) and Coulombic efficiency of a freestanding ATO/C/rGO–LFMP/C/rGO full cell. Performance data are based on the weight of the LFMP cathode.

ranging from 0.2C to 5C (1C = 171 mA g^{-1}_{LFMP}). The full cell thereby reached 130, 118, 108, 98, and 61 mAh g^{-1}_{LFMP} (in the 5th cycle of each individual rate step) at 0.2, 0.5, 1, 2, and 5C, respectively (see also Figure S22, Supporting Information). Furthermore, the cell fully retains its initial capacity when set back to 0.2C, indicating a high stability of the ATO/C/rGO and LFMP/C/rGO full cell configurations. Moreover, the rate performance measurement was also conducted in a two-electrode configuration (Figure S23, Supporting Information), instead of using a three-electrode setup (Figure 7a).

Finally, the cycling stability of ATO/C/rGO–LFMP/C/rGO was analyzed at 1C. In the first cycle, charge and discharge capacities of 118 and 113 mAh g^{-1}_{LFMP} were obtained, respectively, corresponding to a Coulombic efficiency of 95%. In the subsequent cycles, highly stable Coulombic efficiencies of ≥99% were reached. In the 175th cycle, the full cell delivered a discharge capacity of 116 mAh g^{-1}_{LFMP} (Figure 7b), demonstrating the excellent cycling stability of the all-freestanding ATO/C/rGO–LFMP/C/rGO LIB cell.

3. Conclusion

Electrospinning and freeze-casting were tested as possible synthesis routes for the fabrication of freestanding antimony doped SnO_2 (ATO) based hybrid materials. ATO based freestanding composite electrodes have not been reported so far, although this material has demonstrated a very high and stable capacity in conventional electrode design with metal current collectors. Fabrication of ATO/CNFs electrodes by using electrospinning was not possible due to the high pyrolysis temperatures (above 600 °C) required for the carbonization of the PVP matrix, which is accompanied by a reduction of the oxide active material to metallic Sn and a SnSb alloy. The resulting electrodes showed therefore a low specific capacity and rapid capacity fading.

In contrast to electrospinning, freeze-casting enabled a successful fabrication of freestanding ATO electrodes. In a typical synthesis, a suspension containing hydrolyzed tin(IV) and antimony(III) chlorides and GO composites was freeze-cast and finally pyrolyzed resulting in freestanding ATO/rGO composites. Undoped SnO_2/rGO and carbon coated ATO/C/rGO electrodes were prepared in a similar way in a slightly modified procedure. The ATO/C/rGO hybrid material demonstrated a superior rate performance reaching 697 mAh g^{-1} at a high current density of 4 A g^{-1} significantly outperforming the non-coated SnO_2/rGO and ATO/rGO nanocomposites. Moreover, ATO/C/rGO demonstrated an appealing cycling stability retaining 423 mAh g^{-1} after 1000 cycles at 2 A g^{-1}. The distinctly improved electrochemical performance of the freestanding ATO/C/rGO composite is attributed to the synergistic effects of Sb doping, ultrasmall particle size, thin and homogenous carbon coating layer, and good contact between the ATO nanoparticles and the rGO sheets, thus enhancing the electrical conductivity and stabilizing the ATO particles during the electrochemical reactions.

Finally, the freestanding ATO/C/rGO anodes were combined with freestanding $LiFe_{0.2}Mn_{0.8}PO_4$/C/rGO composites employed as cathode to provide a freestanding full cell. The full cell exhibited an excellent cycling stability with practically no capacity decay during 175 cycles at 1C (1C = 171 mAh g^{-1}_{LFMP}), reaching a capacity of 116 mAh g^{-1}_{LFMP} based on the cathode mass. The full cell performance demonstrates the applicability of both ATO/C/rGO and LFMP/C/rGO freestanding electrodes also under more practical conditions.

Based on the obtained results, application of freestanding ATO/C/rGO electrodes seems to be especially favorable for light-weight batteries; applicable, for example, in small electric aerial vehicles at which the gravimetric specific capacity is more important than the volumetric energy density.

4. Experimental Section

Materials: All chemicals were used as-received unless otherwise noted: tin(IV) acetate (Sigma Aldrich), antimony(III) acetate (99.99%, Sigma Aldrich), polyvinylpyrrolidone (PVP; Sigma Aldrich, M_w ≈1300000 by LS), tin (IV) chloride pentahydrate ($SnCl_4 \cdot 5H_2O$; 99%, Sigma Aldrich), L (+)-ascorbic acid ($C_6H_8O_6$, Riedel-de Haen), antimony (III) chloride ($SbCl_3$; 99%, abcr), hydrochloric acid solution (2 м, Bernd Kraft), ammonia solution (25%, Acros), sucrose ($C_{12}H_{22}O_{11}$, Sigma-Aldrich), graphite microparticles (2–15 µm, 99.9995%, Alfa Aesar), PuriEL electrolyte (1.15 м $LiPF_6$ in EC/EMC/DMC = 2:2:6 v/v + 1.0 wt% FEC, soulbrain MI), lithium metal (Rockwood). Sulfuric acid (98%), phosphoric acid (85%), potassium permanganate (99.5%), hydrogen peroxide (30%), barium nitrate (99.5%), and *N*,*N*-dimethylformamide (DMF) were obtained from Penta, Czech Republic.

Synthesis of Graphene Oxide Suspension: A graphene oxide suspension was synthesized according to the authors' previous work[2,52] being a slightly modified synthesis route reported by Marcano et al.[53] 3.0 g graphite and 18.0 mg potassium permanganate were added to a cooled (below 0 °C) mixture of concentrated sulfuric acid (360 mL) and phosphoric acid (40 mL). Afterwards, the mixture was heated at 50 °C for 12 h under stirring, cooled to room temperature and finally poured on ice followed by the addition of a 30% hydrogen peroxide (3.0 mL) solution. After the ice was molten, hydrogen peroxide (30 mL) and water (2500 mL) were subsequently added. The resulting graphene oxide was washed by repeated centrifugation and redispersion in deionized water until a negative reaction on sulfate ions with $Ba(NO_3)_2$ was achieved. The graphene oxide slurry was ultrasonicated for 1 h to exfoliate the GO sheets. The concentration of GO in this suspension was measured to be 20.4 mg mL^{-1} by gravimetric analysis.

Fabrication of ATO/rGO Freestanding Nanocomposites by Freeze-Casting: 263 mg tin(IV) chloride pentahydrate ($SnCl_4{\cdot}5H_2O$; 0.75 mmol), 14 mg antimony(III) chloride ($SbCl_3$; 0.061 mmol), and 30 mg ascorbic acid (1.7 mmol) were dissolved in 5 mL hydrochloric acid (HCl; 2 M). Afterwards 2 mL of the previously prepared GO suspension and 15 mL deionized water were added. The resulting suspension was stirred at room temperature for 20 min followed by the addition of ammonia solution until the pH reached 9 and another stirring period of 45 min. Afterwards, the suspension was washed by repeated centrifugation and redispersion in deionized water. Freestanding nanocomposites were obtained by dispersion of the brown composite material in 20 mL deionized water, subsequent ultrasonic treatment for 2 h and freeze-casting on aluminum blocks, which were cooled in advance with liquid nitrogen. After removing the aluminum substrate, the frozen composite was finally freeze-dried. The resulting freestanding composites were pyrolyzed at 400 °C for 4 h in nitrogen atmosphere yielding ATO/rGO.

ATO/C/rGO and ATO/C-2/rGO composites were prepared similarly except that 20 and 40 mg sucrose was added during ultrasonication, respectively.

Fabrication of ATO/CNF Freestanding Nanocomposites by Electrospinning: In a typical procedure, 1.0 g tin(IV) acetate (2.8 mmol) and 0.1 g antimony(III) acetate (0.33 mmol) were dissolved in 4.5 mL ethanol for 1 day. A second polymer-containing solution was prepared by dissolving 0.3 g PVP in 4.5 mL ethanol. The slightly viscous electrospinning solution was obtained after dropwise addition of the acetate salt-containing solution to the polymer solution. After 1 h of vigorous stirring, the precursor solution was transferred into a syringe having a blunt stainless-steel needle, which was connected to a high voltage power supply. The spun fibers were collected on a rotating (300 rpm) stainless-steel drum collector placed at a distance of 8.5 cm to the needle tip. The electrospinning setup was operated at a voltage difference of 10.2 kV between the needle and the rotating drum collector and a precursor solution feeding rate of 10 mL h^{-1} controlled by a syringe pump.

After electrospinning, the product was carefully removed from the drum collector, resulting in a mechanically stable fiber mat of ≈8 × 20 cm in size that was dried at 80 °C for 1 h, stabilized at 250 °C for 2 h in air, and finally pyrolyzed between 400 and 700 °C in nitrogen for 2 h.

Battery Assembly: Electrochemical measurements were conducted on ECC-PAT-Core electrochemical test cells (EL-Cell). The analyzed freestanding composites were cut into size and used directly as working electrodes, without the addition of extra carbon black or PVDF. The freestanding ATO/rGO, ATO/C/rGO, and SnO_2/rGO electrodes prepared by freeze-casting had a composite mass loading of 1.6–2 mg cm^{-2} and those prepared by electrospinning of 0.9–1.2 mg cm^{-2}. The cells were assembled in an argon filled glove box (Labstar 1250/750, MBraun, Germany) with lithium metal foil as counter and reference electrode, glass fiber membrane (El-CELL ECC1-01-0011-A/L) as separator and a commercial electrolyte consisting of 1.15 M $LiPF_6$ in EC/EMC/DMC at a 2:2:6 vol ratio and 1.0 wt% FEC.

Characterization Methods: Wide angle X-ray diffraction was conducted in transmission mode using a STOE STADI P diffractometer with Cu Kα1-radiation (λ = 1.54060 Å) and a Ge (111) single crystal monochromator equipped with a DECTRIS solid state strip detector MYTHEN 1K. Powder XRD patterns were measured in a 2θ range from 5° to 80° with a step size of 1° and a fixed counting time of 90 s per step.

FTIR measurements were performed on a BXII/1000 FTIR spectrometer (Perkin Elmer) equipped with an ATR unit (Smiths) in the range of 4000–550 cm^{-1}.

TGA measurements were performed on a NETZSCH STA 440 C TG/DSC at a heating rate of 10 °C min^{-1} in a stream of synthetic air of about 25 mL min^{-1}.

XPS measurements were carried out using a VSW TA10 X-ray source providing Al Kα radiation and a VSW HA100 hemispherical analyzer.

Nitrogen sorption measurements were carried out at 77 K using a QUANTACHROME Nova Station C. Before the sorption experiments, the samples were degassed under vacuum for 12 h at 120 °C. The specific surface area was determined by the BET method in the range of p/p = 0.05–0.2. DFT/Monte Carlo methods and a nonlocal DFT adsorption model with slit/cylindrical pores was used to calculate the pore size distribution.

SEM images were acquired with an FEI Helios NanoLab G3 UC scanning electron microscope having a field emission gun operated at 3–5 kV. EDX analysis was conducted at an operating voltage of 20 kV using an X Max^N Silicon Drift Detector with 80 mm^2 detector area (Oxford Instruments) and AZTec acquisition software (Oxford Instruments). The samples were suspended in ethanol and drop-coated on a silicon wafer, which was then glued onto a sample holder with silver lacquer. The freestanding composites were also measured on carbon tabs glued onto a sample holder. Cross-section samples were prepared by gluing the respective composites into a special cross-section holder.

S/TEM measurements were carried out on a FEI Titan Themis equipped with a field emission gun operated at 120 or 300 kV, a high-angle annular dark-field (HAADF) detector and a Super-X energy-dispersive X-ray spectrometer. The samples were dispersed in ethanol and drop-coated on a copper grid with a holey carbon film.

4-point electrical conductivity measurements were carried out on an ECOPIA HMS 3000 system in van der Pauw geometry.

Electrochemical measurements were carried out at 20 °C with ECC-PAT-Core (EL-Cell) battery test cells using an Autolab potentiostat/galvanostat (PGSTAT302N) with a FRA32M module or an Autolab Multipotentiostat M101 equipped with an 8AUT.M101 module operated with Nova 1.11 software. Cyclic voltammetry was conducted in a potential range of 3.0–0.01 V versus Li/Li$^+$ at scan rates of 0.2 and 0.5 mV s^{-1}. Galvanostatic charge/discharge measurements were carried out at different charging and discharging rates varying between 0.2 and 6 A g^{-1} in a voltage window of 3.0–0.01 V. EIS was performed on cells before the cycling test by applying a perturbation voltage of 10 mV in a frequency range of 100 kHz to 0.1 Hz.

Supporting Information

Supporting Information is available from the Wiley Online Library or from the author.

Acknowledgements

The authors thank German Federal Ministry of Education and Research (BMBF), Projects CatSe (Project number 13XP0223A) and Meet HiEnD III (Project number DBA01790), as well as the e-conversion and NIM Excellence Clusters (Deutsche Forschungsgemeinschaft) for financial support. Z.S. was supported by Czech Science Foundation (GACR No. 20–16124J). The authors also acknowledge Tina Reuther for sorption and TGA measurements.

Open access funding enabled and organized by Projekt DEAL.

Conflict of Interest

The authors declare no conflict of interest.

Data Availability Statement

Research data are not shared.

Keywords

cycling stability, freestanding batteries, freestanding electrodes, high capacity, tin oxide

Received: July 2, 2021

---

[1] S. Jiang, R. Huang, W. Zhu, X. Li, Y. Zhao, Z. Gao, L. Gao, J. Zhao, *Front. Chem.* **2019**, *7*, 878.
[2] F. Zoller, K. Peters, P. M. Zehetmaier, P. Zeller, M. Döblinger, T. Bein, Z. k. Sofer, D. Fattakhova-Rohlfing, *Adv. Funct. Mater.* **2018**, *28*, 1706529.
[3] F. Zoller, D. Böhm, T. Bein, D. Fattakhova-Rohlfing, *ChemSusChem* **2019**, *12*, 4140.
[4] Q. Xie, Y. Zhu, P. Zhao, Y. Zhang, S. Wu, *J. Mater. Sci.* **2018**, *53*, 9206.
[5] R. Jia, J. Yue, Q. Xia, J. Xu, X. Zhu, S. Sun, T. Zhai, H. Xia, *Energy Storage Mater.* **2018**, *13*, 303.
[6] B. Jiang, Y. He, B. Li, S. Zhao, S. Wang, Y.-B. He, Z. Lin, *Angew. Chem., Int. Ed.* **2017**, *56*, 1869.
[7] Y. Chen, D. Ge, J. Zhang, R. Chu, J. Zheng, C. Wu, Y. Zeng, Y. Zhang, H. Guo, *Nanoscale* **2018**, *10*, 17378.
[8] K. Peters, P. Zeller, G. Stefanic, V. Skoromets, H. Němec, P. Kužel, D. Fattakhova-Rohlfing, *Chem. Mater.* **2015**, *27*, 1090.
[9] B. Luo, T. Qiu, B. Wang, L. Hao, X. Li, A. Cao, L. Zhi, *Nanoscale* **2015**, *7*, 20380.
[10] L. Gao, G. Wu, J. Ma, T. Jiang, B. Chang, Y. Huang, S. Han, *ACS Appl. Mater. Interfaces* **2020**, *12*, 12982.
[11] X. Liu, J. Guo, T. Liu, J. Zhang, Z. Jia, C. Zhang, *Energy Storage Mater.* **2021**, *35*, 520.
[12] C. Zhang, X. Peng, Z. Guo, C. Cai, Z. Chen, D. Wexler, S. Li, H. Liu, *Carbon* **2012**, *50*, 1897.
[13] Y. Dai, F. Li, Y.-X. Fu, D.-C. Mo, S.-S. Lyu, *RSC Adv.* **2021**, *11*, 8521.
[14] H. Tao, S. Zhu, L. Xiong, X. Yang, L. Zhang, *ChemElectroChem* **2016**, *3*, 1063.
[15] Z. Shen, Y. Hu, Y. Chen, R. Chen, X. He, X. Zhang, H. Shao, Y. Zhang, *Electrochim. Acta* **2016**, *188*, 661.
[16] C. Ma, W. Zhang, Y.-S. He, Q. Gong, H. Che, Z.-F. Ma, *Nanoscale* **2016**, *8*, 4121.
[17] J. Liang, H. Sun, Y. Xu, T. Liu, H. Wang, H. Liu, L. Guo, *Inorg. Chem. Front.* **2019**, *6*, 1367.
[18] J. Liang, H. Sun, Z. Zhao, Y. Wang, Z. Feng, J. Zhu, L. Guo, Y. Huang, X. Duan, *iScience* **2019**, *19*, 728.
[19] B. Wang, J. Ryu, S. Choi, G. Song, D. Hong, C. Hwang, X. Chen, B. Wang, W. Li, H.-K. Song, S. Park, R. S. Ruoff, *ACS Nano* **2018**, *12*, 1739.
[20] S. K. Park, H. K. Kim, K. C. Roh, K. B. Kim, H. S. Park, *CrystEngComm* **2016**, *18*, 6049.
[21] J. Liang, Y. Zhao, L. Guo, L. Li, *ACS Appl. Mater. Interfaces* **2012**, *4*, 5742.
[22] H. Köse, Ş. Dombaycıoğlu, A. O. Aydın, *Int. J. Energy Res.* **2018**, *42*, 4710.
[23] F. R. Bento, P. G. Corradini, L. H. Mascaro, *J. Solid State Electrochem.* **2019**, *23*, 1861.
[24] S. M. Jung, D. W. Kim, H. Y. Jung, *J. Mater. Chem. A* **2020**, *8*, 8244.
[25] S.-I. Oh, J.-C. Kim, D.-W. Kim, *Cellulose* **2019**, *26*, 2557.
[26] J. Ding, Z. Lu, M. Wu, C. Liu, Y. Yang, H. Ji, G. Yang, *Mater. Chem. Phys.* **2018**, *215*, 285.
[27] J. Abe, K. Takahashi, K. Kawase, Y. Kobayashi, S. Shiratori, *ACS Appl. Nano Mater.* **2018**, *1*, 2982.
[28] L. Xia, S. Wang, G. Liu, L. Ding, D. Li, H. Wang, S. Qiao, *Small* **2016**, *12*, 853.
[29] M. Liu, P. Xu, G. Wang, J. Yan, *J. Electron. Mater.* **2019**, *48*, 8206.
[30] X. Min, B. Sun, S. Chen, M. Fang, X. Wu, Y. g. Liu, A. Abdelkader, Z. Huang, T. Liu, K. Xi, R. V. Kumar, *Energy Storage Mater.* **2019**, *16*, 597.
[31] X. Zhang, X. Huang, X. Zhang, L. Xia, B. Zhong, T. Zhang, G. Wen, *Electrochim. Acta* **2016**, *222*, 518.
[32] C. Deng, Y. Liu, Z. Lu, C. Ma, T. Ge, W. Li, G. Yang, *Appl. Surf. Sci.* **2018**, *435*, 1307.
[33] Z. Wang, M. A. Fierke, A. Stein, *J. Electrochem. Soc.* **2008**, *155*, A658.
[34] X. Zhang, X. Huang, D. Liu, T. K. A. Hoang, X. Geng, P. Chen, X. Zhang, G. Wen, *Int. J. Hydrogen Energy* **2018**, *43*, 21428.
[35] P. Dou, Z. Cao, C. Wang, J. Zheng, X. Xu, *Chem. Eng. J.* **2017**, *320*, 405.
[36] X. Zhao, J. Zhang, J. Zhang, C. Gong, X. Gu, Z. Ma, J. Zhou, L. Yu, Z. Zhang, *J. Power Sources* **2015**, *294*, 223.
[37] Z. Xu, W. Yue, X. Yuan, X. Chen, *J. Alloys Compd.* **2019**, *795*, 168.
[38] L. Li, S. He, M. Liu, C. Zhang, W. Chen, *Anal. Chem.* **2015**, *87*, 1638.
[39] D. Song, S. Wang, R. Liu, J. Jiang, Y. Jiang, S. Huang, W. Li, Z. Chen, B. Zhao, *Appl. Surf. Sci.* **2019**, *478*, 290.
[40] E. A. Bondarenko, A. V. Mazanik, E. A. Streltsov, A. I. Kulak, O. V. Korolik, *Mater. Sci. Eng.: B* **2015**, *202*, 61.
[41] L. Liu, M. An, P. Yang, J. Zhang, *Sci. Rep.* **2015**, *5*, 9055.
[42] L. Zhan, X. Zhou, J. Luo, X. Ning, *Ceram. Int.* **2019**, *45*, 6931.
[43] Y.-l. Dong, X.-f. Zhang, X.-l. Cheng, Y.-m. Xu, S. Gao, H. Zhao, L.-h. Huo, *RSC Adv.* **2014**, *4*, 57493.
[44] M.-S. Wang, Z.-Q. Wang, Z.-L. Yang, Y. Huang, J. Zheng, X. Li, *Electrochim. Acta* **2017**, *240*, 7.
[45] N. Mahmood, Y. Hou, *Adv. Sci.* **2014**, *1*, 1400012.
[46] M. Liu, S. Zhang, H. Dong, X. Chen, S. Gao, Y. Sun, W. Li, J. Xu, L. Chen, A. Yuan, W. Lu, *ACS Sustainable Chem. Eng.* **2019**, *7*, 4195.
[47] S. Cui, Z. Wen, E. C. Mattson, S. Mao, J. Chang, M. Weinert, C. J. Hirschmugl, M. Gajdardziska-Josifovska, J. Chen, *J. Mater. Chem. A* **2013**, *1*, 4462.
[48] J. Shin, B. Jeong, J. Kim, V. B. Nam, Y. Yoon, J. Jung, S. Hong, H. Lee, H. Eom, J. Yeo, J. Choi, D. Lee, S. H. Ko, *Adv. Mater.* **2020**, *32*, 1905527.
[49] M. O. Guler, O. Cevher, T. Cetinkaya, U. Tocoglu, H. Akbulut, *Int. J. Energy Res.* **2014**, *38*, 487.
[50] A. Birrozzi, J. Asenbauer, T. E. Ashton, A. R. Groves, D. Geiger, U. Kaiser, J. A. Darr, D. Bresser, *Batteries Supercaps* **2020**, *3*, 284.
[51] L. Ao, C. Wu, X. Wang, Y. Xu, K. Jiang, L. Shang, Y. Li, J. Zhang, Z. Hu, J. Chu, *ACS Appl. Mater. Interfaces* **2020**, *12*, 20824.
[52] F. Zoller, D. Böhm, J. Luxa, M. Döblinger, Z. Sofer, D. Semenenko, T. Bein, D. Fattakhova-Rohlfing, *Mater. Today Energy* **2020**, *16*, 100416.
[53] D. C. Marcano, D. V. Kosynkin, J. M. Berlin, A. Sinitskii, Z. Sun, A. Slesarev, L. B. Alemany, W. Lu, J. M. Tour, *ACS Nano* **2010**, *4*, 4806.